

The applicability of the viscous α -parameterization of gravitational instability in circumstellar disks

E. I. Vorobyov^{a,b},

^a*The Institute for Computational Astrophysics, Saint Mary's University, Halifax, NS, B3H 3C3, Canada*

^b*The Institute of Physics, South Federal University, Stachki 194, Rostov-on-Don, Russia*

Abstract

We study numerically the applicability of the effective-viscosity approach for simulating the effect of gravitational instability (GI) in disks of young stellar objects with different disk-to-star mass ratios ξ . We adopt two α -parameterizations for the effective viscosity based on Lin & Pringle (1990) and Kratter et al. (2008) and compare the resultant disk structure, disk and stellar masses, and mass accretion rates with those obtained directly from numerical simulations of self-gravitating disks around low-mass ($M_* \sim 1.0 M_\odot$) protostars. We find that the effective viscosity can, in principle, simulate the effect of GI in stellar systems with $\xi \lesssim 0.2 - 0.3$, thus corroborating a similar conclusion by Lodato & Rice (2004) that was based on a different α -parameterization. In particular, the Kratter et al's α -parameterization has proven superior to that of Lin & Pringle's, because the success of the latter depends crucially on the proper choice of the α -parameter. However, the α -parameterization generally fails in stellar systems with $\xi \gtrsim 0.3$, particularly in the Class 0 and Class I phases of stellar evolution, yielding too small stellar masses and too large disk-to-star mass ratios. In addition, the time-averaged mass accretion rates onto the star are underestimated in the early disk evolution and greatly overestimated in the late evolution. The failure of the α -parameterization in the case of large ξ is caused by a growing strength of low-order spiral modes in massive disks. Only in the late Class II phase, when the magnitude of spiral modes diminishes and the mode-to-mode interaction ensues, may the effective viscosity be used to simulate the effect of GI in stellar systems with $\xi \gtrsim 0.3$. A simple modification of the effective viscosity that takes into account disk fragmentation can somewhat improve the performance of α -models in the case of large ξ and even approximately reproduce the mass accretion burst phenomenon, the latter being a signature of the early gravitationally unstable stage of stellar evolution (Vorobyov & Basu, 2006). However, further numerical experiments are needed to explore this issue.

Key words: accretion, accretion disks, hydrodynamics, instabilities, stars:

1 Introduction

It has now become evident that circumstellar disks are prone to the development of gravitational instability in the early stage of stellar evolution (e.g. Laughlin & Bodenheimer, 1994; Vorobyov & Basu, 2005; Vorobyov & Basu, 2006; Krumholz et al., 2007; Kratter et al., 2008; Stamatellos & Whitworth, 2008). The non-axisymmetric spiral structure resulting from GI produces gravitational torques, which are negative in the inner disk and positive in the outer disk and help limit disk masses via radial transport of mass and angular momentum (Laughlin et al., 1997; Adams et al., 1989; Vorobyov & Basu, 2005). Even in the late evolution, weak gravitational torques associated with low-amplitude density perturbations in the disk can drive mass accretion rates typical for T Tauri stars (Vorobyov & Basu, 2008).

The fact that gravitational torques trigger mass and angular momentum redistribution in the disk makes them conceptually similar to viscous torques, which are believed to operate in a variety of astrophysical disks. An anticipated question is then whether the GI-induced transport in circumstellar disks can be imitated by some means of effective viscosity? The answer depends on whether mass and angular momentum transport induced by gravitational torques is of global or local nature and this issue still remains an open question.

Lin & Pringle 1987; 1990 were among the first to suggest that the transport induced by GI could be described within a viscous framework and parameterized the effect of GI using the following formulation for the effective kinematic viscosity

$$\nu_{\text{eff}} = \begin{cases} \alpha_{\text{LP}} \left(\frac{Q_c^2}{Q_T^2} - 1 \right) \left(\frac{c_s^2}{\Omega} \right) & \text{if } Q_T \leq Q_c \\ 0 & \text{otherwise,} \end{cases} \quad (1)$$

where Ω is the angular speed, c_s is the sound speed, $Q_T = c_s \Omega / (\pi G \Sigma)$ is the Toomre parameter, Σ is the gas surface density, and Q_c is the critical value of Q_T at which the disk becomes unstable against nonaxisymmetric instability. The dimensionless number α_{LP} represents the efficiency of mass and angular momentum transport by GI. It is evident that Lin & Pringle's

Email address: vorobyov@ap.smu.ca (E. I. Vorobyov).

(1990) parameterization is actually that of Shakura & Sunyaev’s (1973), with α -parameter modified by the term $(Q_c^2/Q_T^2 - 1)$ to describe the effect of GI.

Laughlin & Różyczka (1996) have compared the evolution of a thin, self-gravitating protostellar disk using two-dimensional hydrodynamic simulations with the evolution of a one-dimensional, axisymmetric viscous disk using the model of Lynden-Bell & Pringle (1974). They suggest the following effective α -parameter as a modification to the usual Shakura & Sunyaev α -model

$$\alpha_{\text{LR}} = \frac{\beta\Omega^\zeta}{\Sigma}, \quad (2)$$

where the surface density Σ and angular velocity Ω are in specific units defined in Laughlin & Różyczka (1996), and ζ and β are defined as

$$\zeta = 0.325 - 2.25 \left(\frac{M_*}{M_* + M_d} \right), \quad (3)$$

$$\beta = 0.875 - 4.34\gamma, \quad (4)$$

where M_* and M_d are the star and disk masses, respectively, and γ is the polytropic constant. By considering models with different masses of protostellar disks and different values of Q_T , they concluded that while their parameterization works better than that of Shakura & Sunyaev, the α -prescription fails in relatively massive disks with $M_d \gtrsim 0.5 M_*$ due to the presence of global modes which are not tightly wound. Laughlin & Różyczka’s (1996) parameterization also performs badly in low-mass disks with $M_d \lesssim 0.2 M_*$, overestimating the actual radial mass transport due to gravitational torques. In the intermediate mass regime, however, their parameterization can reproduce the actual gas surface density profiles with a good accuracy. The appearance of dimensional units in the dimensionless coefficient α_{LR} restricts the applicability of equation (2) – one has to either use the Laughlin & Różyczka’s (1996) system of units or redefine equation (2) according to the adopted units.

Lodato & Rice (2004) have studied the applicability of the viscous treatment of the circumstellar disk evolution. They have modelled the evolution of self-gravitating circumstellar disks with masses ranging from 5% to 25% of the star using adiabatic equation of state with $\gamma = 5/3$ and cooling that removes energy on timescales of 7.5 orbital periods. By calculating the gravitational and Reynolds stress tensors and assuming that the sum of these stresses is proportional to the gas pressure, they estimated the effective α -parameter associated with gravitational and Reynolds stresses to be $\alpha_{\text{g,R}} \leq 0.06$ in their numerical simulations. By further assuming that their disks quickly settle in thermal equilibrium (when the rate of viscous energy dissipation is balanced by radiative cooling), they proposed the following expression for the saturated

value of the α -parameter (see also Gammie, 2001)

$$\alpha_{\text{eq}} = \left| \frac{d \ln \Omega}{d \ln r} \right|^{-2} \frac{1}{\gamma(\gamma - 1)t_{\text{cool}}\Omega}, \quad (5)$$

where $t_{\text{cool}} = 7.5\Omega^{-1}$ is a characteristic disk cooling time. For the parameters adopted in Lodato & Rice’s (2004) numerical simulations, $\alpha_{\text{eq}} = 0.05$. A good agreement between numerically derived $\alpha_{\text{g,R}}$ and α_{eq} allowed them to conclude that the viscous treatment of self-gravity is justified in disks with disk-to-star mass ratios $\xi \leq 0.25$ and, perhaps, even in more massive disks (Lodato & Rice, 2005).

Recently, Kratter et al. (2008) have suggested a modification to the usual Shakura & Sunyaev α -model based on the previous numerical simulations of Laughlin & Rózyczka (1996), Lodato & Rice 2004; 2005, and Gammie (2001). Their α -parameter invoked to simulate the effect of GI (α_{GI}) consists of two components: the “short” component α_{short} and “long” component α_{long}

$$\alpha_{\text{GI}} = \left(\alpha_{\text{short}}^2 + \alpha_{\text{long}}^2 \right)^{1/2}, \quad (6)$$

where

$$\alpha_{\text{short}} = \max \left[0.14 \left(\frac{1.3^2}{Q_{\text{T}}^2} - 1 \right) (1 - \mu)^{1.15}, 0 \right] \quad (7)$$

$$\alpha_{\text{long}} = \max \left[\frac{1.4 \times 10^{-3}(2 - Q_{\text{T}})}{\mu^{5/4}Q_{\text{T}}^{1/2}}, 0 \right], \quad (8)$$

where μ is the disk-to-total mass ratio. The “short” component α_{short} differs from the effective α -parameter suggested by Lin & Pringle’s equation (1) only in a mild μ dependence. The “short” and “long” components are meant to represent the different wavelength regimes of the gravitational instability expected to dominate at different values of μ and Q_{T} . We note that Kratter et al. also assumes $Q_{\text{T}} = \max(Q_{\text{T}}, 1)$.

The use of the α -model as a proxy for GI-induced transport has been challenged by Balbus & Papaloizou (1999), who argue that the energy flux of self-gravitating disks is not reducible to a superposition of local quantities such as the radial drift velocity and stress tensor – the essence of an α -disk. Instead, extra terms of non-local nature are present that mostly invalidate the α -approach. Their conclusion is corroborated by recent numerical simulations of collapsing massive cloud cores by Krumholz et al. (2007), who find that gravitational instability in embedded circumstellar disks with masses of order 50% that of the central star is dominated by the $m = 1$ spiral mode induced by

the SLING instability (Adams et al., 1989; Shu et al., 1990). This mechanism is global and enables mass and angular momentum transport on dynamical rather than viscous timescales.

Circumstellar disks form in different physical environments and go through different phases of evolution so that it is quite likely that there is no unique answer on whether GI-induced transport can be described by some means of effective viscosity. Indeed, the early embedded phases of disk evolution (Class 0/I) are substantially influenced by an infalling envelope, both through the mass deposition (Vorobyov & Basu, 2006; Kratter et al., 2008) and envelope irradiation (Matzner & Levin, 2005; Cai et al., 2008). Younger Class 0/I disks are usually more massive than in the older Class II ones (Vorobyov, 2009). As a result, gravitational instabilities in Class 0/I disk may be dominated by low-order ($m \leq 2$), large-amplitude global modes (see e.g. Krumholz et al., 2007), which are likely to invalidate the viscous approach. On the other hand, Class II disks evolve in relative isolation and settle into a steady state that is characterized by low-amplitude, high-order modes $m \geq 3$ (e.g. Lodato & Rice, 2004; Vorobyov & Basu, 2007). Such modes tend to produce more fluctuations and cancellation in the net gravitational torque on large scales, thus making the viscous approach feasible.

The mass and angular momentum transport in self-gravitating disks is difficult to deal with analytically due to a kaleidoscope of competing spiral modes. Furthermore, long-term multidimensional numerical simulations of the evolution of circumstellar disks involving an accurate calculation of disk self-gravity are usually very computationally intensive. On the other hand, the theory of viscous accretion disks is fairly well developed (e.g. Pringle, 1981) and is relatively easy to deal with numerically. This motivated many authors to use the viscous approach to mimic the effect of gravitational instability when studying the long-term evolution of circumstellar disks (e.g. Lin & Pringle, 1990; Nakamoto & Nakagawa, 1995; Hueso & Guillot, 2005; Dullemond et al., 2006; Kratter et al., 2008). It is therefore important to know if and when the viscous approach is applicable. Some work in this direction has already been done by Lodato & Rice 2004; 2005 and Cossins et al. (2009), who considered a short-term evolution of isolated disks with different disk-to-star mass ratios meant to represent different stellar evolution phases. However, they have not considered a long-term disk evolution due to an enormous CPU time demand of fully three-dimensional simulations. In the present paper we explore the applicability of the α -parameterization of gravitational instability along the entire stellar evolution sequence, starting from a deeply embedded Class 0 phase and ending with a late Class II phase (T Tauri phase). Although the T Tauri phase of stellar evolution is likely to harbour only marginally gravitationally unstable disks with associated torques of low intensity (Vorobyov & Basu, 2007), the disk structure may bear the imprints of the early, GI-dominated phase. That is why it is important to capture the main stages of

disk evolution altogether in one numerical simulation. We focus on the α -parameterizations of Lin & Pringle (1990) and Kratter et al. (2008) and defer a study of the Lodato & Rice’s (2004) parameterization to a follow-up paper. Contrary to other studies, we run our numerical simulations of circumstellar disks first with self-gravity calculated accurately by solving the Poisson integral and then with self-gravity imitated by effective viscosity. We then perform a detailed analysis of the resultant circumstellar disk structure, masses, and mass accretion rates in the both approaches.

2 Description of numerical approach

2.1 Main equations

We seek to capture the main evolution phases of a circumstellar disk altogether, starting from the deeply embedded Class 0 phase and ending with the T Tauri phase. This can be accomplished only by adopting the so-called thin-disk approximation. In this approximation, the basic equations for mass and momentum transport are written as (Vorobyov & Basu, 2006; Vorobyov & Basu, 2009)

$$\frac{\partial \Sigma}{\partial t} = -\nabla_p \cdot (\Sigma \mathbf{v}_p), \quad (9)$$

$$\Sigma \frac{d\mathbf{v}_p}{dt} = -\nabla_p \mathcal{P} + \Sigma \mathbf{g}_p^d + \Sigma \mathbf{g}_p^s + (\nabla \cdot \mathbf{\Pi})_p, \quad (10)$$

where Σ is the mass surface density, $\mathcal{P} = \int_{-Z}^Z P dz$ is the vertically integrated form of the gas pressure P , Z is the radially and azimuthally varying vertical scale height, $\mathbf{v}_p = v_r \hat{\mathbf{r}} + v_\phi \hat{\phi}$ is the velocity in the disk plane, $\nabla_p = \hat{\mathbf{r}} \partial / \partial r + \hat{\phi} r^{-1} \partial / \partial \phi$ is the gradient along the planar coordinates of the disk, and $\mathbf{g}_p^{d,s} = g_r^{d,s} \hat{\mathbf{r}} + g_\phi^{d,s} \hat{\phi}$ is the gravitational acceleration in the disk plane. The latter consists (in general) of two parts: that due to the disk self-gravity (\mathbf{g}_p^d) and that due to the gravity of the central star (\mathbf{g}_p^s). The gravitational acceleration \mathbf{g}_p^d is found by solving for the Poisson integral (Vorobyov & Basu, 2006). The viscous stress tensor $\mathbf{\Pi}$ is expressed as

$$\mathbf{\Pi} = 2\Sigma \nu_{\text{eff}} \left(\nabla v - \frac{1}{3} (\nabla \cdot v) \mathbf{e} \right), \quad (11)$$

where ∇v is a symmetrized velocity gradient tensor, \mathbf{e} is the unit tensor, and ν_{eff} is the effective kinematic viscosity. The components of $(\nabla \cdot \mathbf{\Pi})_p$ in polar coordinates (r, ϕ) can be found in Vorobyov & Basu (2009). We emphasize that

we do not take any simplifying assumptions about the form of the viscous stress tensor, apart from those imposed by the adopted thin-disc approximation. It can be shown (Lodato, 2008) that equation (10) can be reduced to the usual equation for the conservation of angular momentum of a radial annulus in the axisymmetric viscous accretion disc (Pringle, 1981).

Equations (9) and (10) are closed with a barotropic equation that makes a smooth transition from isothermal to adiabatic evolution at $\Sigma = \Sigma_{\text{cr}} = 36.2 \text{ g cm}^{-2}$:

$$\mathcal{P} = c_s^2 \Sigma + c_s^2 \Sigma_{\text{cr}} \left(\frac{\Sigma}{\Sigma_{\text{cr}}} \right)^\gamma, \quad (12)$$

where $c_s = 0.188 \text{ km s}^{-1}$ is the sound speed in the beginning of numerical simulations and $\gamma = 1.4$. Assuming a local vertical hydrostatic equilibrium in the disk, $\Sigma_{\text{cr}} = 36.2 \text{ g cm}^{-2}$ becomes equivalent to the critical number density 10^{-11} cm^{-3} (Masunaga & Inutsuka, 2005).

The thin-disc approximation is an excellent means to calculate the evolution for many orbital periods and many model parameters. It is well justified as long as the aspect ratio $A \equiv A(r)$ of the disk vertical scale height Z to radius r does not considerably exceed 0.1. The aspect ratio $A(r)$ for a Keplerian disk is usually approximated by the following expression

$$A \leq C Q_{\text{T}} M_{\text{d}}(r) / M_*, \quad (13)$$

where $M_{\text{d}}(r)$ is the disk mass contained *within* radius r and C is a constant, the actual value of which depends on the gas surface density distribution Σ in the disk. For a disk of constant surface density, C is equal unity. However, circumstellar disks are characterized by surface density profiles declining with radius. For the scaling $\Sigma \propto r^{-1.5}$ typical for our disks, $C = 1/4$. Adopting further $Q_{\text{T}} = 2.0$ and $M_{\text{d}}(r) / M_* = 0.5$, which are the upper limits in our numerical simulations, we obtain the maximum value of $A(r) = 0.25$. This analysis demonstrates that the thin-disc approximation may be only marginally valid in the outer regions of a circumstellar disk, but is certainly justified in its inner regions where $M_{\text{d}}(r) / M_*$ is small. A typical distribution of the aspect ratio A in a disk around one solar mass star was shown in figure 7 in Vorobyov (2009).

2.2 Initial conditions

We start our numerical integration in the pre-stellar phase, which is characterized by a collapsing (flat) starless cloud core, and continue into the late

accretion phase, which is characterised by a protostar-disk system. This ensures a self-consistent formation of a circumstellar disk, which occupies the innermost portion of the computational grid, while the infalling envelope (in the embedded stage of stellar evolution) occupies the rest of the grid.

We consider model cloud cores with mass $M_{\text{cl}} = 1.5 M_{\odot}$, initial temperature $T = 10 K$, mean molecular weight 2.33, and the outer radius $r_{\text{out}} = 0.07 \text{ pc}$. The initial radial surface density and angular velocity profiles are characteristic of a collapsing axisymmetric magnetically supercritical core (Basu, 1997):

$$\Sigma = \frac{r_0 \Sigma_0}{\sqrt{r^2 + r_0^2}}, \quad (14)$$

$$\Omega = 2\Omega_0 \left(\frac{r_0}{r}\right)^2 \left[\sqrt{1 + \left(\frac{r}{r_0}\right)^2} - 1 \right], \quad (15)$$

where Ω_0 is the central angular velocity. The scale length $r_0 = kc_s^2/(G\Sigma_0)$, where $k = \sqrt{2}/\pi$ and $\Sigma_0 = 0.12 \text{ g cm}^{-2}$. These initial profiles are characterized by the important dimensionless free parameter $\eta \equiv \Omega_0^2 r_0^2 / c_s^2$ and have the property that the asymptotic ($r \gg r_0$) ratio of centrifugal to gravitational acceleration has magnitude $\sqrt{2}\eta$ (Basu, 1997). The centrifugal radius of a mass shell initially located at radius r is estimated to be $r_{\text{cf}} = j^2/(Gm) = \sqrt{2}\eta r$, where $j = \Omega r^2$ is the specific angular momentum.

The strength of gravitational instability is expected to depend on the disk mass. According to Lodato & Rice (2004,2005), a viscous parameterization of GI is allowed in systems with the disk-to-star mass ratio $\xi \lesssim 0.25$ but may fail in systems with relatively more massive disks. It is therefore important to consider systems with different disk-to-star mass ratios. This can be achieved by varying the initial rate of rotation of a model cloud core, but keeping all other cloud core characteristics fixed. Indeed, an increase in Ω_0 would result in a larger value of η and r_{cf} . In turn, an increase in the centrifugal radius r_{cf} would result in more mass landing onto the disk rather than being accreted directly onto the central star (plus some inner circumstellar region at $r < 5 \text{ AU}$ which is unresolved in our numerical simulations), thus raising the resultant disk-to-mass ratio. According to Caselli et al. (2002), velocity gradients in dense molecular cloud cores range between 0.5 and $6.0 \text{ km s}^{-1} \text{ pc}^{-1}$. Therefore, we choose three typical values for the central angular velocity of our model cloud cores: $\Omega = \Omega_{0,1} = 0.82 \text{ km s}^{-1} \text{ pc}^{-1}$, $\Omega = \Omega_{0,2} = 1.5 \text{ km s}^{-1} \text{ pc}^{-1}$, and $\Omega = \Omega_{0,3} = 2.5 \text{ km s}^{-1} \text{ pc}^{-1}$. It is convenient to parameterize our models in terms of the ratio of rotational to gravitational energy β , which is very similar in magnitude to the parameter η introduced above. Caselli et al. (2002) report β ranging between 10^{-4} and 0.07 in their sample of dense molecular cloud cores. Our model cloud cores have $\beta_1 = 8.83 \times 10^{-4}$, $\beta_2 = 2.3 \times 10^{-3}$, and

$\beta_3 = 8.2 \times 10^{-3}$. For the sake of conciseness, we present the results of the β_1 and β_3 models, referring to the intermediate β_2 model only where necessary.

Equations (9), (10), (12) are solved in polar coordinates (r, ϕ) on a numerical grid with 128×128 cells. We use the method of finite differences with a time-explicit, operator-split solution procedure. Advection is performed using the second-order van Leer scheme. The radial points are logarithmically spaced. The innermost grid point is located at $r_{\text{in}} = 5$ AU, and the size of the first adjacent cell is 0.3 AU. We introduce a “sink cell” at $r < 5$ AU, which represents the central star plus some circumstellar disk material, and impose a free inflow inner boundary condition. The sink cell is dynamically inactive but serves as the source of gravity, thereby influencing the gas dynamics in the active computational grid. The outer boundary is reflecting. The gravity of a thin disk is computed by directly summing the input from each computational cell to the total gravitational potential. The convolution theorem is used to speed up the summation. A small amount of artificial viscosity is added to the code to smear out shocks over one computational zone according to the usual von Neumann & Richtmyer’s (1950) prescription, though the associated artificial viscosity torques were shown to be negligible in comparison with gravitational torques (Vorobyov & Basu, 2007). A more detailed explanation of numerical methods and relevant tests can be found in Vorobyov & Basu 2006; 2007.

2.3 Three numerical models

We consider three numerical models that are distinct in the way the right-hand side of equation (10) is handled. In the first model (hereafter, self-gravitating model or SG model), viscosity is set to zero throughout the entire evolution (forth term) and the system evolves exclusively via gravity of the disk and central star (second and third terms, respectively), as well as pressure forces (first term). In the second model (hereafter, Lin and Pringle model or LP model), the disk self-gravity is switched off after the disk formation (no second term) and the subsequent evolution is governed by pressure forces (first term), gravity of the central star (third term), viscosity (forth term). In particular, the kinematic viscosity is computed using the following representation

$$\nu_{\text{eff}} = \begin{cases} \alpha_{\text{LP}} \left(\frac{Q_c^2}{Q_T^2} - 1 \right) c_s h & \text{if } Q_T \leq Q_c \\ 0 & \text{otherwise,} \end{cases} \quad (16)$$

where h is the disk scale height. The latter is calculated assuming the vertical hydrostatic equilibrium in the gravitational field of the disk and the central star (see Vorobyov, 2009). For numerical reasons, ν_{eff} is set to zero if Q_T drops accidentally below some low value, which is set in our simulations to 0.3. The

third model (hereafter, KMK model) differs from the second model only in the way the effective viscosity is defined. More specifically, we use the following expression for the effective kinematic viscosity

$$\nu_{\text{eff}} = \alpha_{\text{GI}} c_s h, \quad (17)$$

where α_{GI} is determined from equation (6). Following Kratter et al. (2008), we also set $Q_{\text{T}} = \max(Q_{\text{T}}, 1)$. In Section 6, we consider a modification to the KMK model that attempt to deal with the fragmentation regime at $Q_{\text{T}} < 1.0$. All the three numerical models start from identical initial conditions as described in Section 2.2

3 Cloud cores with low rates of rotation.

In this section we consider model cloud cores that are described by the ratio of rotational to gravitational energy $\beta \equiv \beta_1 = 0.88 \times 10^{-3}$. This value is chosen to represent dense cloud cores with low rates of rotation, as inferred from the measurements of Caselli et al. (2002).

3.1 The LP model

Equation (16) indicates that the LP model has two free parameters: α_{LP} and Q_{cr} . It is therefore our main purpose to determine the values of α_{LP} , using which the LP model reproduces best the exact solution provided by the SG model. We have found that the LP model depends only weakly on Q_{cr} , as soon as its value is kept near 1.5. In this study we set $Q_{\text{cr}} = 1.7$. We vary α_{LP} in wide limits, starting from 10^{-4} and ending with 0.5. Figures 1-3 show the disk radial structure obtained in the SG model (solid lines) and LP model (dashed lines). More specifically, the top panels show the radial gas surface density distributions, while the middle and bottom panels show the radial profiles of the gas temperature and Toomre parameter Q_{T} , respectively. It may not be entirely consistent to calculate Q_{T} in the non-self-gravitating model. Nevertheless, this quantity may serve as an indicator of how far the stability properties of the LP model deviate from the exact solution. Three characteristic times based on the age of the central star in the SG model have been chosen: $t = 0.2$ Myr (left row), $t = 1.0$ Myr (middle row), and $t = 2.0$ Myr (right row). The left row represents an evolution stage when about 25% of the initial cloud core material is still contained in the infalling envelope, while the middle and right rows represent a stage when the envelope has almost vanishes. Three values of the α -parameter have been selected for the presentation: $\alpha_{\text{LP}} = 10^{-4}$ (Fig. 1), $\alpha_{\text{LP}} = 0.01$ (Fig. 2), and $\alpha_{\text{LP}} = 0.25$ (Fig. 3).

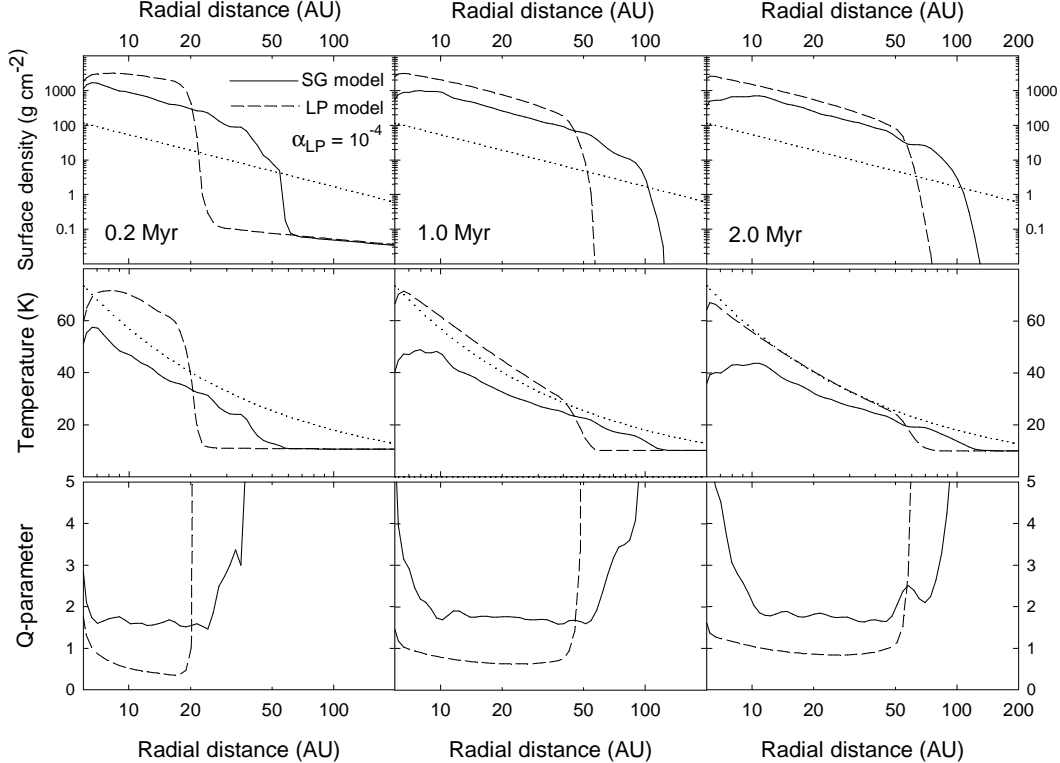


Fig. 1. Gas surface density (top row), gas temperature (middle row), and Q -parameter (bottom row) as a function of radius in the $\alpha_{LP} = 10^{-4}$ model (dashed lines) and SG model (solid lines). Three distinct evolutionary times since the formation of the central protostar are indicated in each column. The dotted lines show the MMSN gas surface density profile (top row) and a gas temperature profile typical for circumstellar disk (middle row) as inferred by AW05.

The dotted lines show the minimum mass solar nebular (MMSN) density profile $\Sigma = 1.7 \times 10^3 (r/1\text{AU})^{-1.5}$ (Hayashi, 1985) and a disk radial temperature profile $T = 180 (r/1\text{AU})^{-0.5}$ inferred by Andrews & Williams (2005) (hereafter AW05) from a large sample of YSO in the Taurus-Aurigae star-forming region.

It is instructive to review the main disk properties obtained by the SG model. An accurate determination of disk masses in numerical simulations of collapsing cloud cores is not a trivial task. Self-consistently formed circumstellar disks have a wide range of masses and sizes, which are not known *a priori*. In addition, they often experience radial pulsations in the early evolution phase, which makes it difficult to use such tracers as rotational support against gravity of the central star. However, numerical and observational studies of circumstellar disks indicate that the disk surface density is a declining function of radius. Therefore, we distinguish between disks and infalling envelopes using a critical surface density for the disk-to-envelope transition, for which we choose a fiducial value of $\Sigma_{\text{tr}} = 0.1 \text{ g cm}^{-2}$. This choice is dictated by the fact that densest *starless* cores have surface densities only slightly lower than the adopted value of Σ_{tr} . In addition, our numerical simulations indicate that self-gravitating

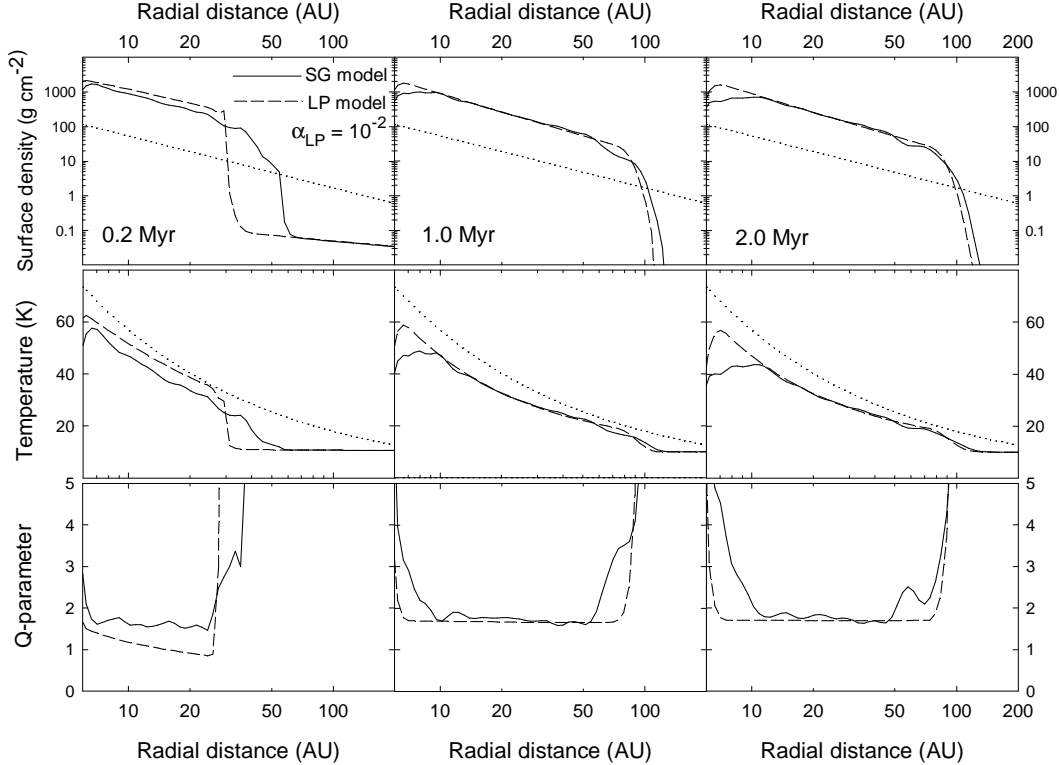


Fig. 2. The same as Fig. 1 only for the $\alpha_{LP} = 10^{-2}$ model.

disks have sharp outer edges and the gas densities of order $0.01 - 0.1 \text{ g cm}^{-2}$ characterize a typical transition region between the disk and envelope.

As the solid lines in Figs 1-3 indicate, most of the self-gravitating disk is characterized by a power-law surface density distribution declining with radius as $r^{-1.5}$. This slope is also predicted by the MMSN hypothesis (Hayashi, 1985). However, our obtained gas surface densities are almost a factor of 10 greater than those of the MMSN throughout the entire disk evolution. This feature is an important property of self-gravitating disks (see also Vorobyov & Basu, 2009). It makes easier giant planets to form, because planet formation scenarios seem to require gas densities at least a few times larger than those of the minimum-mass disk (Ida & Lin, 2004; Boss, 2001). The radial gas temperature profiles indicate that the self-gravitating disk is somewhat colder than the typical disk in Taurus-Aurigae region (AW05). This is particularly true in the late evolution, though large deviations from the typical profile toward colder disk are also present in the AW05 sample. We point out that irradiation by a central source can raise the disk temperature and seriously affect the disk propensity to fragmentation in the inner disk regions (e.g. Matzner & Levin, 2005). Unfortunately, this effect is difficult to take into account self-consistently in polytropic disks due to the lack of detailed treatment of cooling and heating. Hotter disk can be obtained in our numerical simulations by choosing a larger value for the ratio of specific heats γ in the barotropic equation of state (12). We discuss hotter disks in Section 5. We

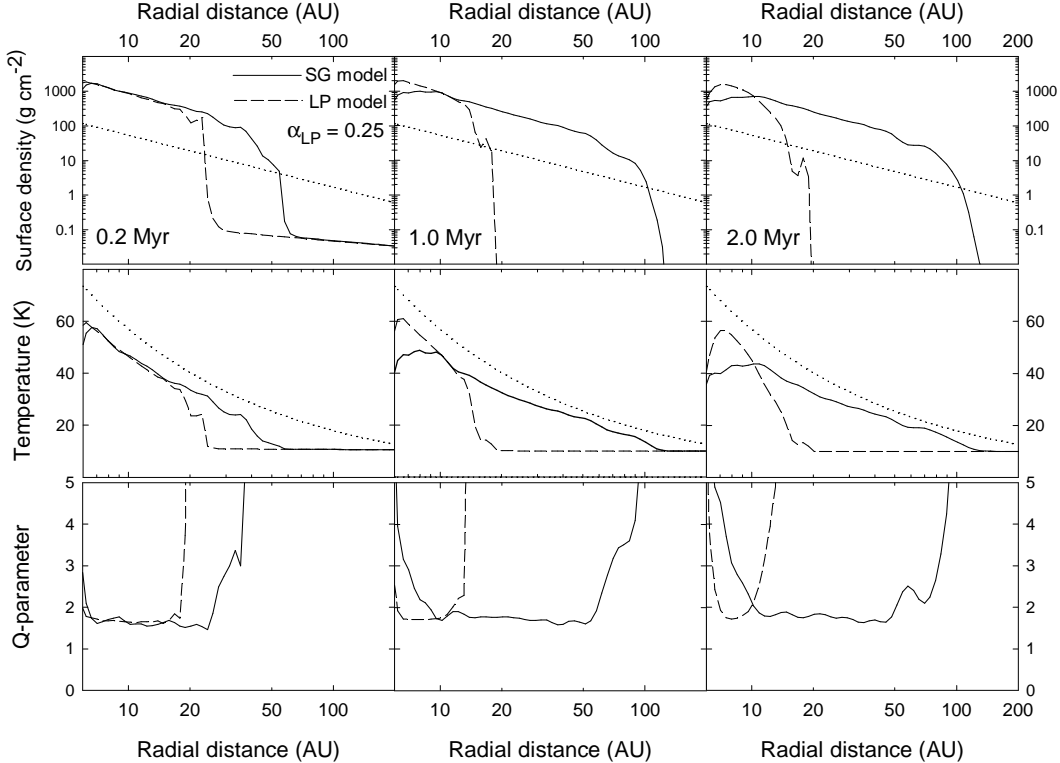


Fig. 3. The same as Fig. 1 only for the $\alpha_{LP} = 0.25$ model.

also note that our self-gravitating disk exhibits a near-Keplerian rotation.

Finally, the time behaviour of the Toomre parameter Q_T in a self-gravitating disk warrants some attention. It is evident that the self-gravitating disk regulates itself near the boundary of gravitational stability, with values of Q_T lying in the 1.7 – 2.0 range. This important property breaks down when a sufficient amount of physical viscosity (i.e. due to turbulence) is present in the disk (see e.g. Vorobyov & Basu, 2009). We note that the Q -parameter in the early evolution of a self-gravitating disk may occasionally drop below 1.7 – 2.0 in some parts of the disk. These episodes are usually associated with disk fragmentation and formation of dense clumps, which have masses of up to 10–20 Jupiters, sizes of several AU, number densities of up to $10^{13} - 10^{14} \text{ cm}^{-3}$ and are pressure supported against their own gravity. Most of these clumps are quickly driven onto the central protostar by gravitational torques from spiral arms. This phenomenon causes a burst of mass accretion (Vorobyov & Basu, 2005; Vorobyov & Basu, 2006) and is very transient in nature (the burst itself takes less than 100 yr). A small number of the clumps may be flung into the outer regions where they disperse, most likely due to a combined action of tidal forces, differential rotation, and insufficient numerical resolution (our grid is logarithmically spaced in the radial direction).

We now proceed with comparing the disk structure in the SG and LP models. Figures 1-3 reveal that both the $\alpha_{LP} = 10^{-4}$ model and $\alpha_{LP} = 0.25$ model

fail to accurately reproduce the radial structure of the disk obtained in the SG model. More specifically, the $\alpha_{\text{LP}} = 10^{-4}$ model yields too dense and hot disks throughout the entire evolution. The disagreement is particularly strong in the early disk evolution ($t = 0.2$ Myr), when the radial gas surface density distribution becomes substantially shallower than that predicted by the exact solution ($\propto r^{-1.5}$). The obtained disk radii in the $\alpha_{\text{LP}} = 10^{-4}$ model are smaller by a factor of 2 – 3 than those found in the SG model. The Toomre parameter is also considerably smaller than that of the self-gravitating disk. In summary, the LP model with α_{LP} as small as 10^{-4} fails to provide an acceptable fit to the exact solution.

When we turn to large values of the α -parameter $\alpha_{\text{LP}} = 0.25$ (Fig 3), the corresponding LP model seems to yield density and temperature profiles that are in acceptable agreement with those of the exact solution only in the very early phase of disk evolution ($t = 0.2$ Myr). Even in this early stage, the disk size is severely underestimated. Furthermore, the late evolution sees a strong mismatch between the disk structure in the LP and SG models. We conclude that large values of $\alpha_{\text{LP}} \gtrsim 0.25$ may be marginally acceptable in the early, strongly gravitationally unstable phase of disk evolution, but cannot be used to simulate the effect of self-gravity on long time scales of order of several Myr.

The $\alpha_{\text{LP}} = 10^{-2}$ model (dashed lines in Fig. 2) appears to provide the best fit to the exact solution. Although in the early disk evolution ($t = 0.2$ Myr) the simulated gas surface densities and temperatures are somewhat larger than those provided by the SG model, in the late evolution ($t \gtrsim 1$ Myr) they are almost indistinguishable from the exact solution throughout most of the disk. We conclude that the LP model can be rather successful in reproducing the effect of gravitational instability in star-disk systems formed from slowly rotating cloud cores, provided that the value of α_{LP} lies close to 10^{-2} .

It is interesting to compare disk and stellar masses obtained in the LP models with those of the SG model. The left column in Fig. 4 shows the stellar mass (top), disk mass (middle), and disk-to-star mass ratio ξ (bottom) for the SG and LP models. More specifically, the solid, dashed, dash-dotted, and dotted lines present data for the SG model, $\alpha_{\text{LP}} = 10^{-4}$ model, $\alpha_{\text{LP}} = 10^{-2}$ model, and $\alpha_{\text{LP}} = 0.25$ model, respectively. We use $\Sigma_{\text{crit}} = 0.1 \text{ g cm}^{-2}$ for the disk-to-envelope transition. The horizontal axis shows time elapsed since the formation of the central star. The disk forms at $t = 0.14 \text{ Myr}$ ¹, when the central object has accreted approximately 60% of the initial cloud core mass $M_{\text{cl}} = 1.5 M_{\odot}$. The disk-to-star mass ratio in the SG model never exceeds $\xi = 17\%$. It is

¹ In fact, the disk forms earlier but its evolution is unresolved in the inner 5 AU due to the use of a sink cell in our numerical simulations. However, the mass contained in this inner 5 AU is negligible compared to the rest of the resolved disk.

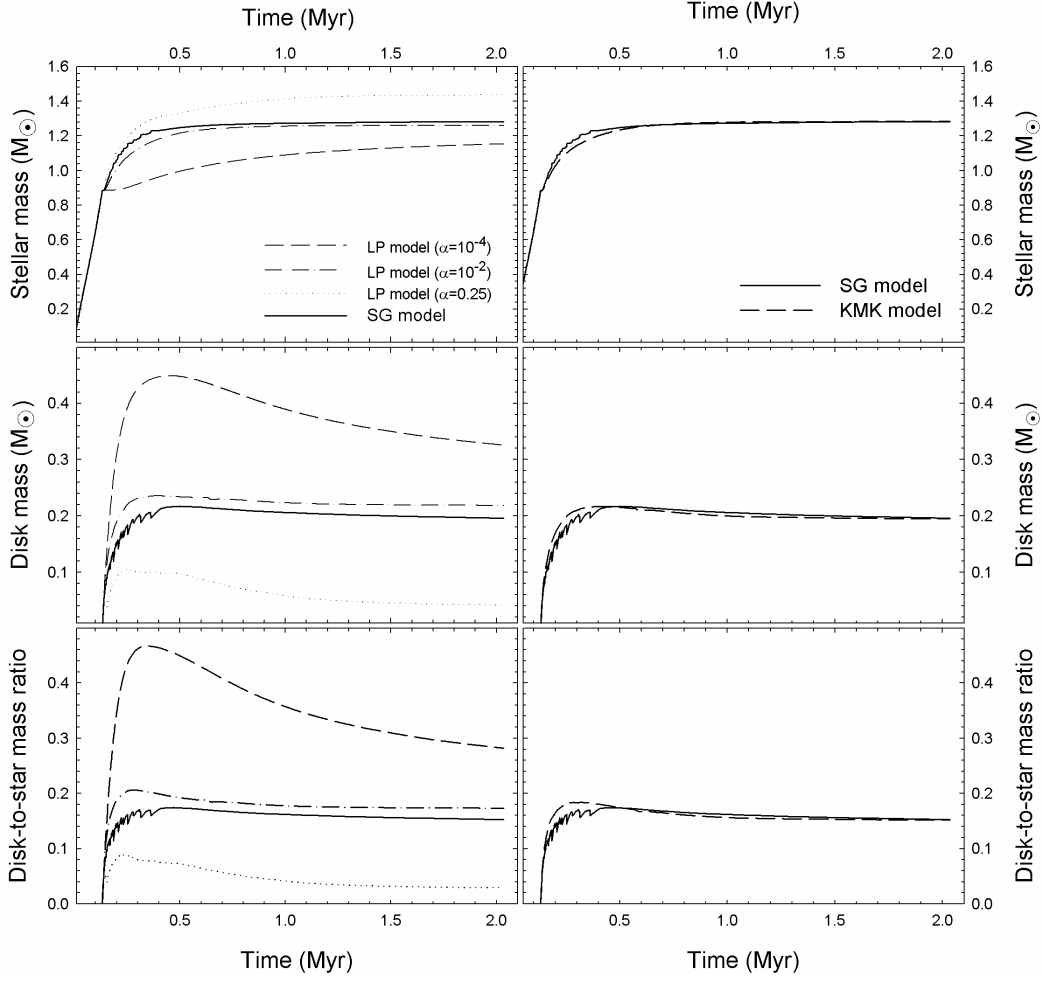


Fig. 4. Stellar masses (top row), disk masses (middle row), and disk-to-star mass ratios (bottom row) in the LP model (left column) and KMK model (right column). In particular, the dashed, dash-dotted, and dotted lines in the left column present data for the $\alpha_{\text{LP}} = 10^{-4}$ model, $\alpha_{\text{LP}} = 10^{-2}$ model, and $\alpha_{\text{LP}} = 0.25$ model, respectively, while the dashed line in the right column shows data for the KMK model. The solid lines in both columns correspond to the SG model.

evident that the $\alpha_{\text{LP}} = 10^{-2}$ model yields the masses and disk-to-star mass ratios that agree best with those derived in the SG model. The high-viscosity LP model ($\alpha_{\text{LP}} = 0.25$) predicts too large values for the stellar mass and too low values for the disk mass, whereas the low-viscosity LP model ($\alpha_{\text{LP}} = 10^{-4}$) does it vice versa. This example nicely illustrates the sensitivity of the LP model to the choice of α_{LP} .

Finally, we calculate the instantaneous mass accretion rates through the inner disk boundary as $\dot{M} = -2\pi r_{\text{in}} \Sigma v_r$, where $r_{\text{in}} = 5$ AU, and v_r is the radial gas velocity at r_{in} . There is evidence that accretion on to the star is a highly variable process in the early embedded stage of disk evolution. Observations indicate that, in addition to young stellar objects (YSOs) with mass accretion

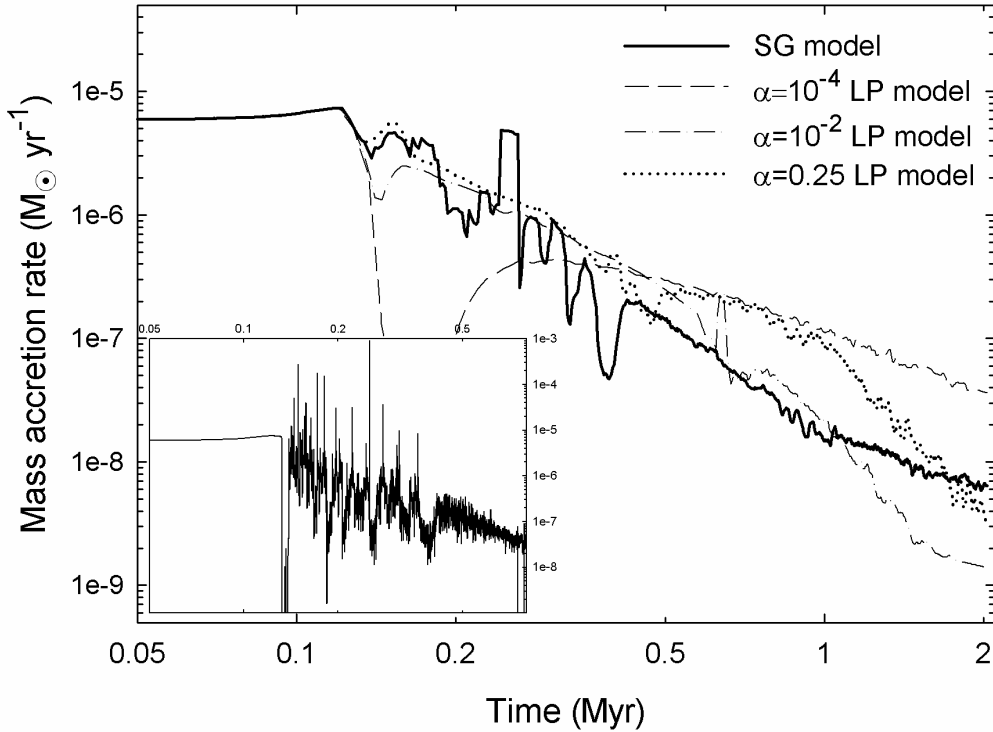


Fig. 5. Time-averaged mass accretion rates in the SG model (solid line), $\alpha_{LP} = 10^{-4}$ LP model (dashed line), $\alpha_{LP} = 10^{-2}$ LP model (dash-dotted line), and $\alpha_{LP} = 0.25$ LP model (dotted line). The insert shows the instantaneous mass accretion rate versus time in the SG model.

rates similar to those predicted by Shu (1977), there is a substantial populace of YSOs with the sub-Shu accretion rates $\dot{M} \leq 10^{-6} M_{\odot} \text{ yr}^{-1}$ (Enoch et al., 2009) and a small number of super-Shu accretors with $\dot{M} > 10^{-5} M_{\odot} \text{ yr}^{-1}$. Furthermore, numerical simulations show that the disk in the early embedded phase becomes periodically destabilized due to the mass deposition from an infalling envelope (Vorobyov & Basu, 2005; Vorobyov & Basu, 2006; Boley, 2009). The resulted gravitational torques drive excess mass in the form of dense clumps on to the central star, thus producing the so-called burst phenomenon (Vorobyov & Basu, 2005; Vorobyov & Basu, 2006). This phenomenon can only be captured approximately by any model that mimics mass transport in self-gravitating disks via an effective viscosity (see e.g. Kratter et al., 2008). In Section 6, we try to reproduce the burst behaviour within the framework of the KMK model by modifying the definition of the α -parameter.

In order to smooth out the bursts and facilitate a comparison between the SG and LP models, we calculate the mean mass accretion rates $\langle \dot{M} \rangle$ by time-averaging the instantaneous rates over 2×10^4 yr. Figure 5 shows $\langle \dot{M} \rangle$ versus time for the SG model (solid line), $\alpha_{LP} = 10^{-4}$ LP model (dashed line), $\alpha_{LP} =$

10^{-2} LP model (dash-dotted line), and $\alpha_{\text{LP}} = 0.25$ LP model (dotted line). The horizontal axis shows time elapsed since the formation of the central star. The burst phenomenon is illustrated in the insert to Fig. 5, which shows the instantaneous mass accretion rates in the SG model as a function of time. It is seen that the time-averaged mass accretion rates are identical before the disk formation ($t \leq 0.14$ Myr) but become distinct soon afterward. Even after time-averaging, some substantial variations in the mass accretion rate of the SG model are still visible. It is evident that the $\alpha_{\text{LP}} = 10^{-4}$ LP model greatly underestimates $\langle \dot{M} \rangle$ in the early 0.4 Myr, while considerably overestimating it in the subsequent evolution. The high-viscosity $\alpha_{\text{LP}} = 0.25$ LP model also seem to produce larger accretion rates than those of the exact solution, especially in the late phase. The $\alpha_{\text{LP}} = 10^{-2}$ LP model, again, demonstrates better agreement with the exact solution, though somewhat underestimating $\langle \dot{M} \rangle$ after 1 Myr.

3.2 The KMK model

In this section we investigate the efficiency of the Kratter et al.'s (2008) α -parameterization in simulating the effect of GI in circumstellar disks. The KMK model described by equations (6)-(8) is more useful and flexible than the LP model because the former has no free parameters² and it includes a mild dependence on the disk-to-total mass ratio μ . This ratio is expected to depend on the initial rate of rotation of a molecular cloud core and may considerably vary along the sequence of stellar evolution phases, and therefore could be an important ingredient for successful modeling of the effect of GI in circumstellar disks. For a more detailed discussion we refer the reader to Kratter et al. (2008).

Figure 6 shows radial profiles of the gas surface density (top), temperature (middle), and Toomre parameter (bottom) obtained in the KMK model (dashed lines) and in the SG model (solid lines). The horizontal axis, as usual, shows time elapsed since the formation of the central star. Three characteristic stellar ages, as indicated in each row, are chosen for the presentation. It is evident that the KMK model shows a satisfactory performance, particularly in the late evolution stage. In the early evolution, the predicted disk surface densities and temperatures are slightly larger than those of the SG model, but the difference is not significant. Comparing Figs 2 and 6 one can see that the KMK model reproduces the exact solution to the same extent and accuracy as the best $\alpha_{\text{LP}} = 10^{-2}$ LP model. However, the supremacy of the KMK model is obvious – it has no free parameters to adjust. We believe that the KMK

² In fact, the value of the critical Toomre parameter Q_c is set to 1.3 in the Kratter et al.'s approach.

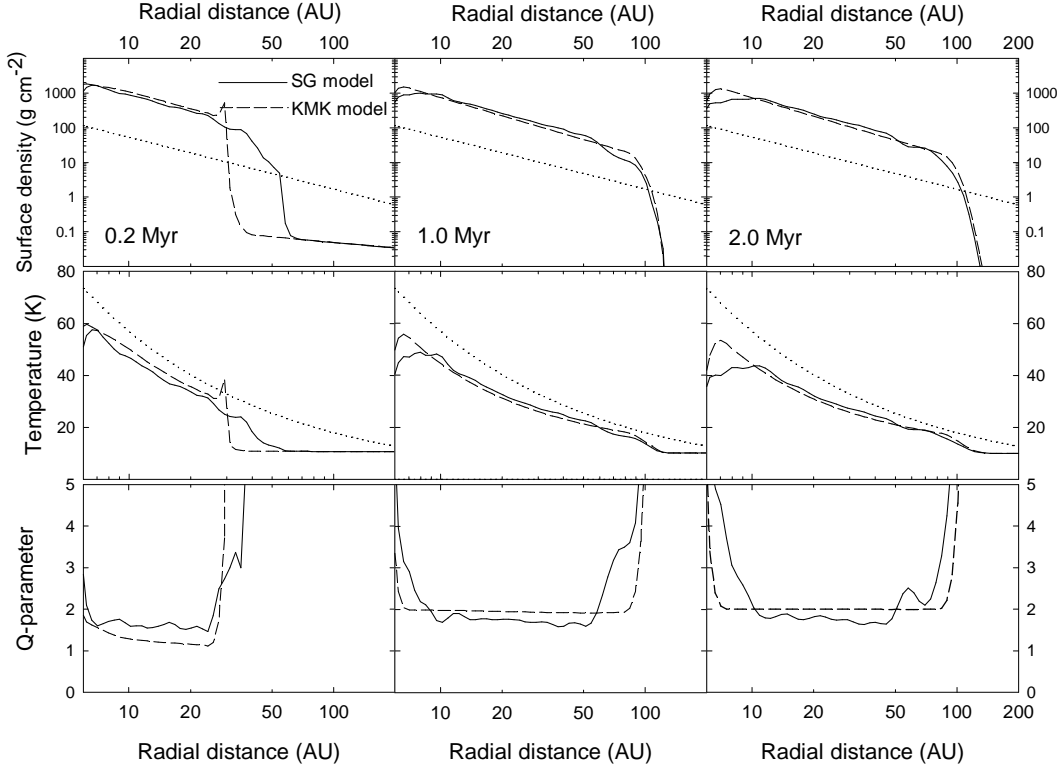


Fig. 6. Gas surface density (top row), gas temperature (middle row), and Q -parameter (bottom row) as a function of radius in the KMK model (dashed lines) and SG model (solid lines). Three distinct evolutionary times since the formation of the central protostar are indicated in each column. The dotted lines show the MMSN gas surface density profile (top row) and a typical gas temperature profile (middle row), as inferred for circumstellar disks by AW05

model owes its success to the use of a two-component α -parameter, α_{GI} .

The right column in Fig. 4 shows the stellar mass (top), disk mass (middle), and disk-to-star mass ratio ξ obtained using the KMK model (dashed lines) and SG model (solid lines). This figure demonstrates that the KMK model yields the disk and stellar masses that are in good agreement with those of the SG model. We conclude that both the LP and KMK models can, in principle, reproduce the radial structure of self-gravitating disks, time-averaged accretion rates, and masses in star/disk systems formed from slowly rotating cloud cores with $\beta \lesssim 1.0 \times 10^{-3}$. Such systems are characterized by disk-to-star mass ratios not exceeding $\xi = 0.2$. The α -parameterization in such systems appears to be justified. The agreement with the exact solution is somewhat modest in the early evolution but improves considerably in the late evolution as the strength of gravitational instability declines. In the case of LP model, the α -parameter has to be set to $\alpha_{LP} \approx 0.01$.

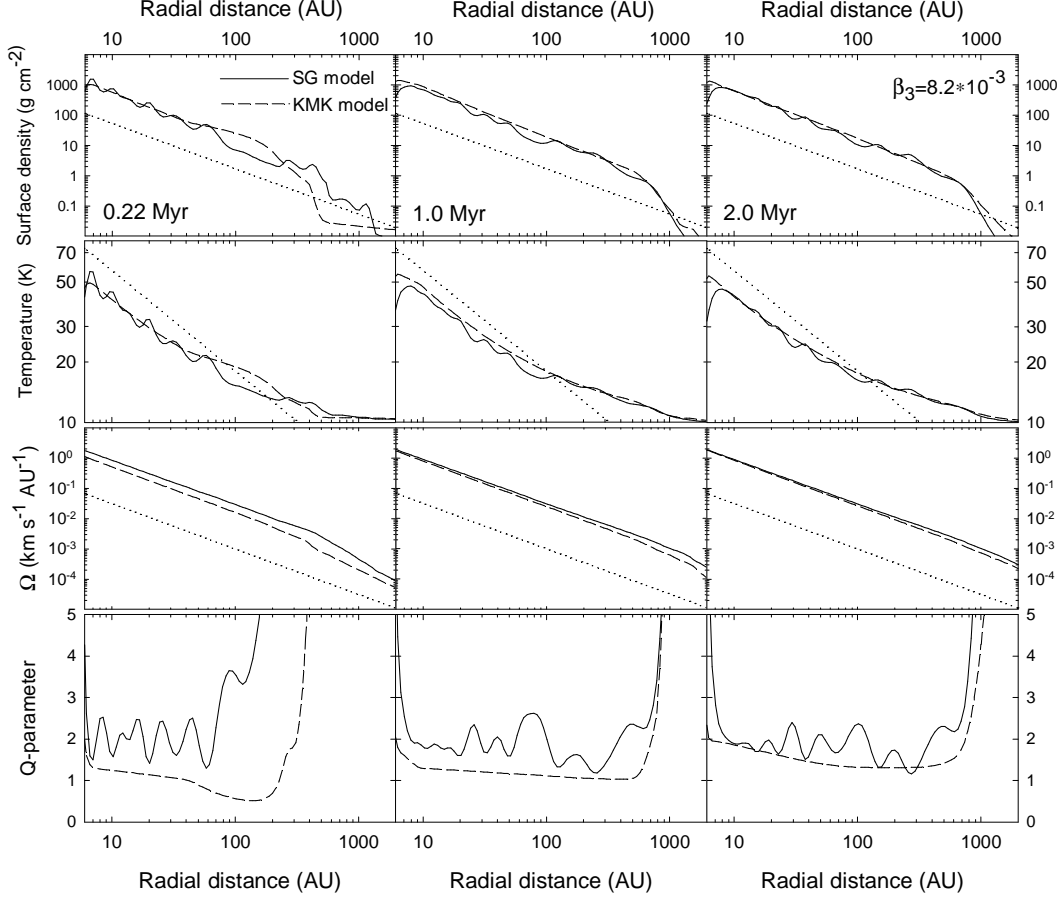


Fig. 7. From top to bottom: gas surface density, gas temperature, angular velocity, and Q -parameter as a function of radius in the KMK model (dashed lines) and SG model (solid lines) for the $\beta_3 = 8.2 \times 10^{-3}$ case. Three distinct evolutionary times since the formation of the central protostar are indicated in each column. The dotted lines show the MMSN gas surface density profile (first row), typical gas temperature profile (second row) as inferred in circumstellar disks by AW05, and a Kepler rotation law (third row).

4 Cloud cores with intermediate and high rates of rotation.

In this section we consider cloud cores that are characterized by the ratios of rotational to gravitational energy $\beta_2 = 2.3 \times 10^{-3}$ and $\beta_3 = 8.2 \times 10^{-3}$, with most attention being concentrated on the latter case. Since the KMK model has proven superior in comparison to the LP model, we focus on the former one, summarizing the main results for the LP model where necessary. Cloud cores with high rates of rotation are expected to yield disks with large disk-to-star mass ratios. Our motivation is then to determine the extent to which the KMK model can reproduce the exact solution in systems with disk-to-star mass ratios considerably larger than that of the previous section, $\xi \sim 0.17$.

Figure 7 compares the disk radial structure obtained in the SG model (solid

lines) and KMK model (dashed lines) for the β_3 case. The layout of the figure is exactly the same as in Fig. 1, but we have also plotted the radial distribution of the angular velocity Ω in the third row from top. The dotted line in this row shows a Kepler rotation law, $\Omega \propto r^{-1.5}$.

Both the approximate and exact solutions are characterized by similar slopes of the gas surface density $\Sigma \propto r^{-1.5}$, gas temperature $T \propto r^{-0.4}$, and angular velocity $\Omega \propto r^{-1.5}$. One can see that the KMK model reproduces the radial gas surface densities and temperatures but yields too low angular velocities and the Toomre parameter, especially in the early evolution. This implies that the KMK model underestimates the mass of the central star.

The failure of the KMK model to accurately reproduce stellar masses is illustrated in Fig. 8, which show the stellar masses (top row), disk masses (middle row), and disk-to-star mass ratios (bottom row) for the SG model (solid lines) and KMK model (dashed lines). In particular, the left column corresponds to the β_2 case, while the right column presents the β_3 case. The horizontal axis shows time elapsed since the formation of the central star. To compare masses along the sequence of stellar evolution phases, we need an evolutionary indicator to distinguish between Class 0, Class I, and Class II phases. We use a classification of André et al. (1993), who suggest that the transition between Class 0 and Class I objects occurs when about 50% of the initial cloud core is accreted onto the protostar-disk system. The Class II phase is consequently defined by the time when the infalling envelope clears and its total mass drops below 10% of the initial cloud core mass M_{cl} . The vertical dotted lines mark the onset of Class I (left line) and Class II (right line) phases. A general trend of the KMK model to *underestimate* the stellar masses and to *overestimate* the disk-to-star mass ratios is clearly seen.

To quantify this mismatch between the models, we calculate time-averaged stellar masses $\langle M_* \rangle$, disk masses $\langle M_{\text{d}} \rangle$, and disk-to-star mass ratios $\langle \xi \rangle$ in each major stellar evolution phase. The resulted values are listed in Table 1. It is evident that the mismatch between the SG model and KMK model is particularly strong in the Class 0 and Class I phases. For instance, the β_3 KMK model yields $\langle \xi \rangle = 1.31$ in the Class I phase, which is almost a factor of 3 larger than the corresponding value for the SG model. The disagreement in the Class II phase is in general less intense than in the Class 0 and Class I phases. Somewhat surprisingly, disk masses in the KMK model differ insignificantly from those of the SG model. The $\alpha_{\text{LP}} = 10^{-2}$ model shows a very similar behaviour.

Our numerical simulations demonstrate that the extent to which the KMK model departs from the SG model is direct proportional to the value of β , and hence to the disk-to-star mass ratio. This is not surprising. Disks in systems with greater ξ are more gravitationally unstable, and the viscous approach is

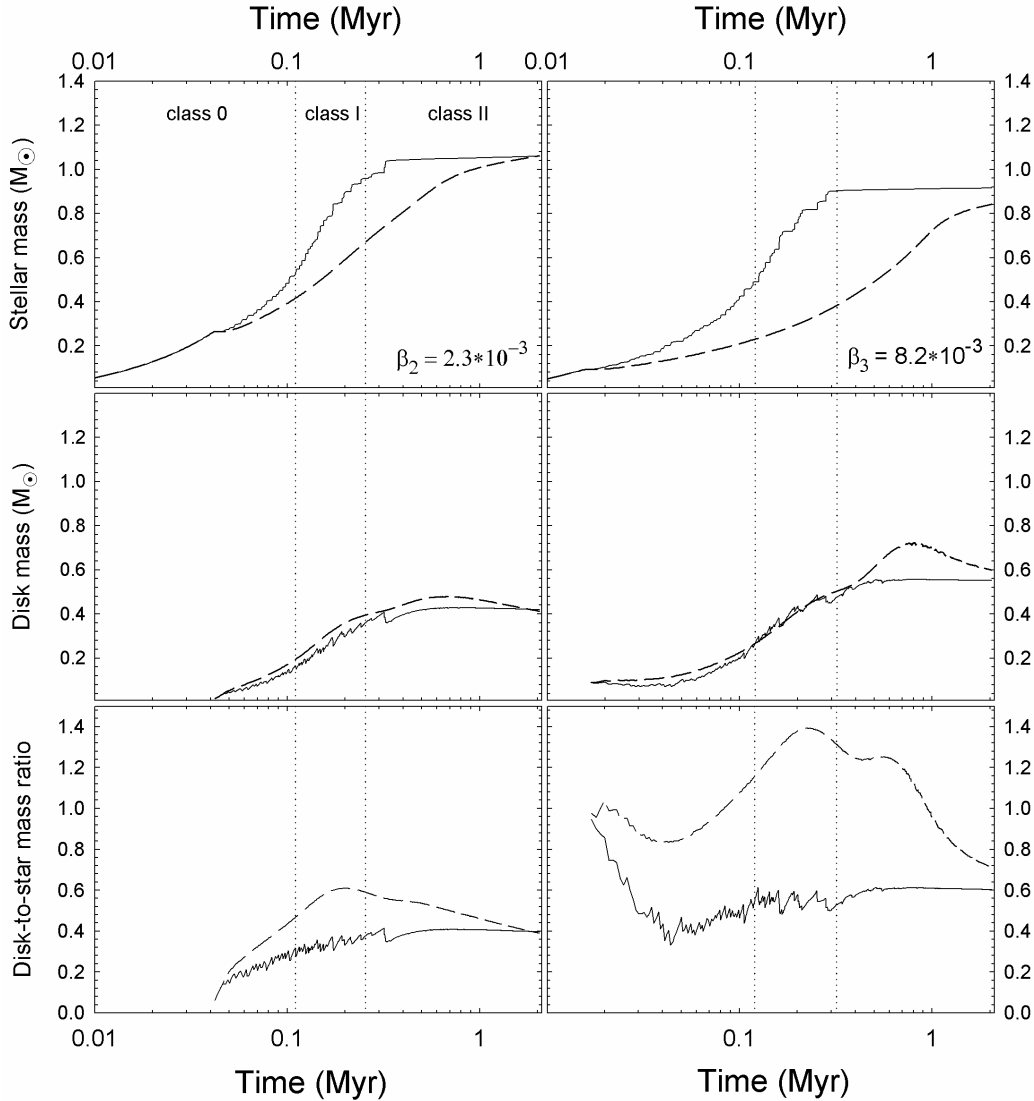


Fig. 8. Time evolution of stellar masses (top row), disk masses (middle row), and disk-to-star mass ratios (bottom row) in the KMK model (dashed lines) and SG model (solid lines). The left and right columns correspond to the $\beta_2 = 2.3 \times 10^{-3}$ and $\beta_3 = 8.2 \times 10^{-3}$ cases, respectively. The horizontal axis shows time since the formation of the central star.

Table 1

SG model versus KMK model for $\beta_2 = 2.3 \times 10^{-3}$ and $\beta_3 = 8.2 \times 10^{-3}$

phase	$\langle M_* \rangle_{\beta_2}$	$\langle M_d \rangle_{\beta_2}$	$\langle \xi \rangle_{\beta_2}$	$\langle M_* \rangle_{\beta_3}$	$\langle M_d \rangle_{\beta_3}$	$\langle \xi \rangle_{\beta_3}$
Class 0	0.39/0.33	0.09/0.12	0.23/0.33	0.29/0.17	0.14/0.17	0.49/0.97
Class I	0.81/0.56	0.28/0.33	0.34/0.58	0.77/0.31	0.42/0.42	0.54/1.33
Class II	1.05/0.98	0.42/0.44	0.4/0.46	0.91/0.71	0.55/0.64	0.6/0.94

All mean masses are in M_\odot . The slash differentiates between the SG model (left) and KMK model (right).

expected to fail in massive disks, which are dominated by global spiral modes of low order (see e.g. Lodato & Rice, 2005; Krumholz et al., 2007). We illustrate this phenomenon by calculating the global Fourier amplitudes (GFA) defined as

$$C_m(t) = \frac{1}{M_d} \left| \int_0^{2\pi} \int_{r_{\text{in}}}^{r_{\text{disc}}} \Sigma(r, \phi, t) e^{im\phi} r dr d\phi \right|, \quad (18)$$

where M_d is the disc mass and r_{disc} is the disc’s physical outer radius. The instantaneous GFA show considerable fluctuations and we have to time-average them over 2×10^4 yr in order to produce a smooth output. The time evolution of the time-averaged GFA (log units) is shown in Fig. 9 for the $\beta_1 = 0.88 \times 10^{-3}$ SG model (top), $\beta_2 = 2.3 \times 10^{-3}$ SG model (middle), and $\beta_3 = 8.2 \times 10^{-3}$ SG model (bottom). Each color type corresponds to a mode of specific order, as indicated in the legend

The time behaviour of the GFA is indicative of two qualitatively different stages in the disk evolution. In the early stage ($t \lesssim 1.0$ Myr), a clear segregation between the modes is evident – the lower order mode dominates its immediate higher order neighbour in all models. In particular, the $m = 1$ mode is almost always the strongest one³. The modes also show a clear tendency to decrease in magnitude with time. In the late stage, however, this clear picture breaks into a kaleidoscope of low-magnitude modes competing for dominance with each other. These mode fluctuations are not a numerical noise but are rather caused by ongoing low-amplitude non-axisymmetric density perturbations sustained by swing amplification at the disk’s sharp outer edge. As was shown by Vorobyov & Basu (2007), self-gravity of the disk is essential for these density perturbations to persist into the late disk evolution. The density perturbations quickly disappear if self-gravity is switched off.

The visual analysis of GFA in the early stage reveals that models with greater β are characterized by spiral modes of greater magnitude. For instance, the magnitude of the $m = 1$ mode at $t = 0.5$ Myr in the β_1 model is $C_1 = -1.9$ dex, while β_2 and β_3 models have $C_1 = -1.7$ dex and $C_1 = -1.5$ dex, respectively. What is more important is that the relative strength of the low-order modes ($m \leq 2$) is greater in models with greater β (and greater ξ). These facts, when taken altogether, account for the failure of the viscous approach in systems with $\xi \gtrsim 0.2$. The preponderance of strong low-order modes, which are global in nature, largely invalidates the local-in-nature viscous approach. When we

³ In the present paper, we have ignored a possible wobbling of the central star, which may increase the strength of the odd modes, especially that of the $m = 1$ mode (Adams et al., 1989; Shu et al., 1990). Numerical hydrodynamics simulations with the indirect potential in the momentum equation (10) are needed to accurately assess the strength of this effect.

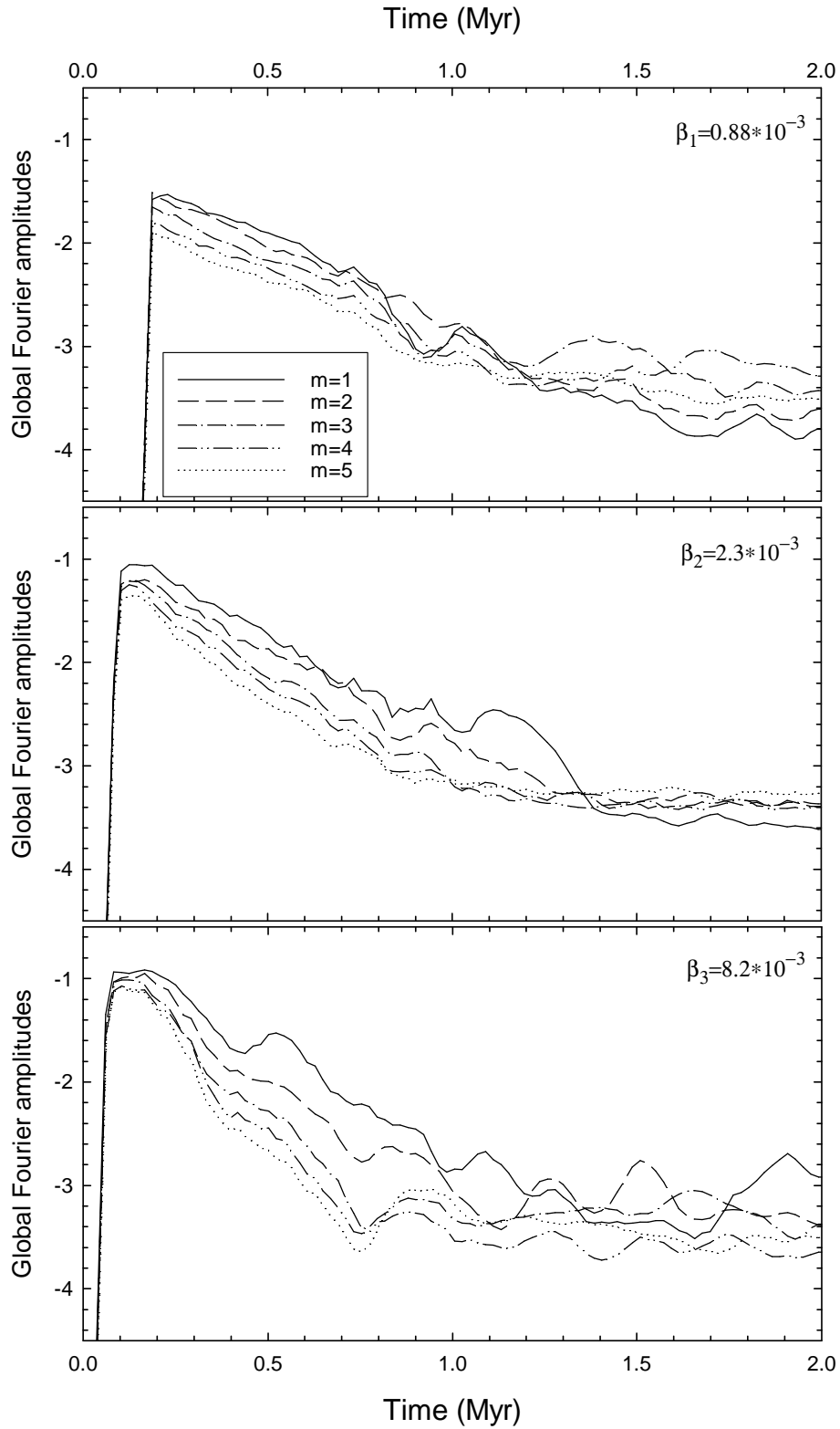


Fig. 9. Global Fourier amplitudes (averaged over 2×10^4 yr) in the $\beta_1 = 0.88 \times 10^{-3}$ SG model (top), $\beta_2 = 2.3 \times 10^{-3}$ SG model (middle), and $\beta_3 = 8.2 \times 10^{-3}$ SG model (bottom). The horizontal axis shows time elapsed since the formation of the central star. Each line type corresponds to a mode of specific order, as indicated in the legend.

turn to the late stage at $t \gtrsim 1$ Myr, we see that all modes saturate at a considerably lower value of order $C = -3.5$ dex. Moreover, characteristic fluctuations tend to produce more cancellation in the net gravitational torque on large scales, thus making the GI-induced transport localwise. This explains why the KMK model performs better in the late stage.

Finally, we present in Figure 10 the time-averaged mass accretion rates $\langle \dot{M} \rangle$ as a function of time for the $\beta_2 = 2.3 \times 10^{-3}$ case (top-left panel) and $\beta_3 = 8.2 \times 10^{-3}$ case (top-right panel). In particular, the solid and dashed lines correspond to the SG model and KMK model, respectively. The time-averaged values are obtained from the instantaneous mass accretion rates by applying a running average method over 2×10^4 yr. For comparison, the bottom row presents $\langle \dot{M} \rangle$ versus time for the $\beta_1 = 0.88 \times 10^{-3}$ case. More specifically, the dashed line in the bottom-left panel corresponds to the best $\alpha_{\text{LP}} = 10^{-2}$ LP model, while the same line type in the bottom-right panel presents the KMK model. In both bottom panels, the solid line shows the data for the SG model. The horizontal axis shows time elapsed since the beginning of numerical simulations.

The central star forms in all models at around 0.05 Myr, when $\langle \dot{M} \rangle$ increases sharply to a maximum value of $\sim 10^{-5} M_{\odot} \text{ yr}^{-1}$. A period of near constant accretion then ensues, when the matter is accreted directly from the infalling envelope onto the star. This stage may be very short (or even evanescent) in systems with high rates of rotation (top panels) due to almost instantaneous onset of a disk formation stage. In this stage, the matter is first accreted onto the disk and through the disk onto the star, and the mass accretion rate is highly variable. It is evident that the β_2 and β_3 KMK models (top row) underestimate $\langle \dot{M} \rangle$ in the early disk evolution, while considerably overestimating $\langle \dot{M} \rangle$ in the late evolution. This explains why viscous models with large ξ tend to greatly underestimate stellar masses in the Class 0 and Class I phases. It appears that viscous torques in massive disks fail to keep up with gravitational torques in the early, strongly gravitationally unstable phase but drive too high rates of accretion in the late, gravitationally quiescent phase. On the other hand, the bottom row in Fig. 10 indicates that viscous models with low rates of rotation and small disk-to-star mass ratios ($\beta \lesssim 1 \times 10^{-3}$ and $\xi \lesssim 0.2$) show a better fit to the SG model, departing from the exact solution only by a factor of several.

5 Higher disk temperature

Observations and numerical simulations suggest that circumstellar disks are characterized by a variety of physical conditions, including vastly different disk sizes, disk-to-star mass ratios, and temperature profiles (see e.g. Andrews &

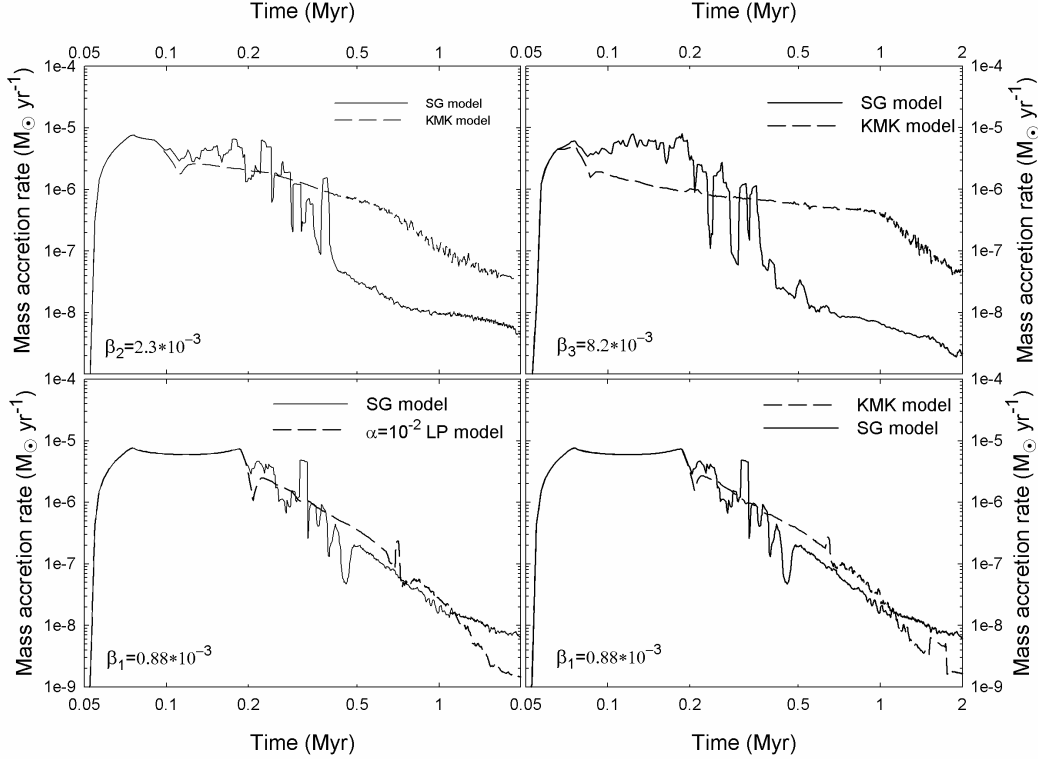


Fig. 10. Mass accretion rates $\langle \dot{M} \rangle$ (averaged over 2×10^4 yr) versus time. The top row shows $\langle \dot{M} \rangle$ for $\beta_2 = 2.3 \times 10^{-3}$ (top-left panel) and $\beta_3 = 8.2 \times 10^{-3}$ (top-right panel). In particular, the solid and dashed lines correspond to the SG and KMK models, respectively. The bottom row presents $\langle \dot{M} \rangle$ for the $\beta_1 = 0.88 \times 10^{-3}$ case. More specifically, the dashed lines in the left and right panels show the data for the $\alpha_{\text{LP}} = 10^{-2}$ LP model and KMK model, respectively, while the solid lines in both low panels present the data for the SG model.

Williams, 2005; Vorobyov, 2009). We have considered the effect of different disk-to-star mass ratios in the previous sections. However, it is also important to consider disks with different temperatures, since this is one of the factors that control the disk propensity to gravitational instability and fragmentation. In our polytropic approach, we can increase the disk temperature by raising the ratio of specific heats γ . In a real disk, the rise in γ does not necessarily result in higher temperatures due to a strong dependence on cooling and heating terms. These effects are not considered in the present study.

Figure 11 presents the disk radial structure for the $\gamma = 5/3$ and $\beta_3 = 8.2 \times 10^{-3}$ case. The dashed and solid lines show the data obtained in the KMK model and SG model, respectively. The layout of the figure is identical to that of Fig. 7. The comparison of Fig. 7 and Fig. 11 reveals that the $\gamma = 5/3$ disk is characterized by roughly a factor of 2 greater gas temperature than that of the $\gamma = 1.4$ disk. In fact, the $\gamma = 5/3$ disk has temperatures that systematically exceed typical temperatures inferred by AW05 for a sample of circumstellar disks (dotted line in the second row). Nevertheless, the performance of the

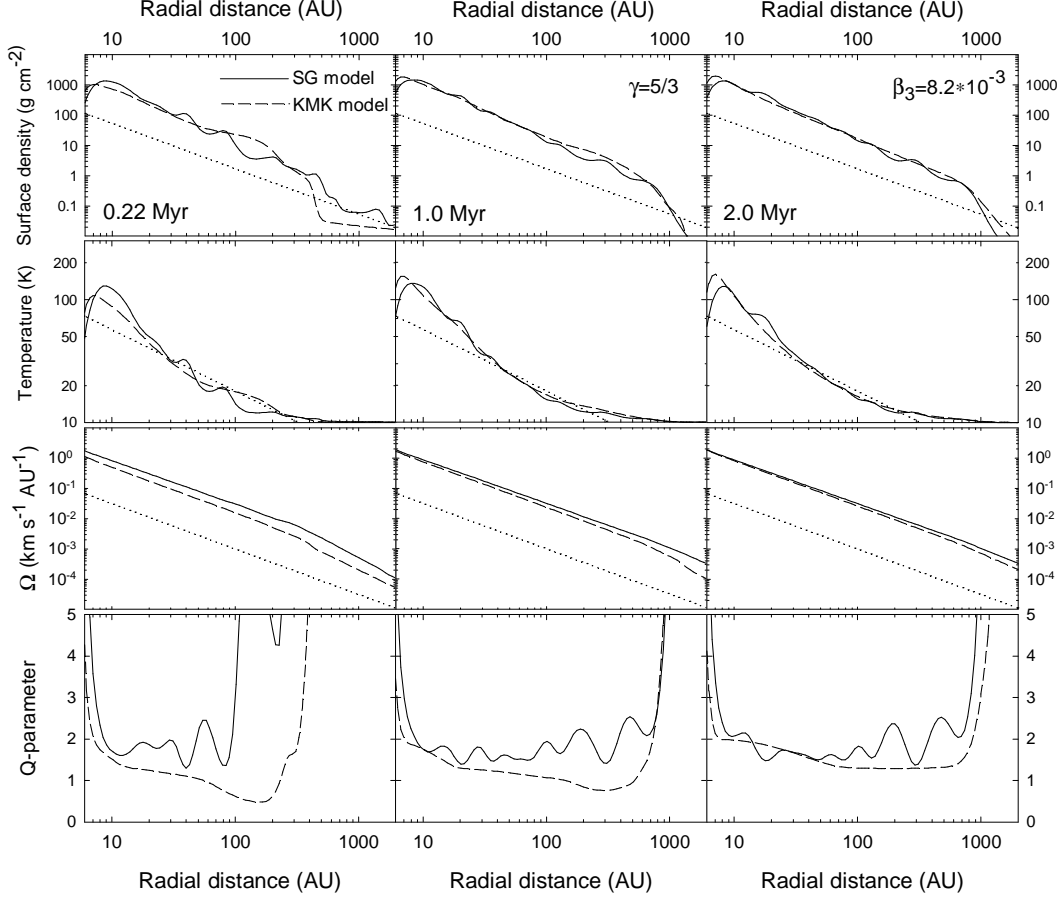


Fig. 11. The same as Figure 7 only for the $\gamma = 5/3$ disk.

KMK model is largely unaffected by this change in the disk temperature. As in the $\gamma = 1.4$ case, the KMK model yields too low angular velocities in the early evolution (third row), thus underestimating stellar masses. In general, the temporal behaviour of disk masses, stellar masses, and disk-to-star mass ratios is very similar to that shown in Fig. 8 for the $\gamma = 1.4$ disk. This is not unexpected. Disk and stellar masses are largely determined by the mass accretion rate onto the star. As Vorobyov & Basu (2009) have demonstrated, a factor of 2 increase in the disk temperature makes little effect on the time-averaged mass accretion rates, though it may alter the temporal behaviour of the instantaneous mass accretion rates.

6 Disk fragmentation

When the local Toomre parameter Q_T drops below some critical value $Q_{cr,f}$, which is often equal or close to 1.0, fragmentation in a circumstellar disk ensues. To account for this qualitatively different regime of disk evolution,

Kratter et al. (2008) have defined a critical surface density

$$\Sigma_{\text{cr},f} = \frac{c_s \Omega}{\pi G Q_{\text{cr},f}} \quad (19)$$

and assumed that fragmentation depletes the disk surface density when $Q_{\text{T}} < Q_{\text{cr},f}$ at a rate

$$\dot{\Sigma}_f = -(\Sigma - \Sigma_{\text{cr},f})\Omega. \quad (20)$$

According to Kratter et al. (2008), this rate is fast enough to ensure that Q_{T} never dips appreciably below $Q_{\text{cr},f}$. The actual dynamics of the fragments is not followed, instead they are allowed to accrete on to the star at a rate $\dot{M}_{*,f} = 0.05 M_f \Omega$.

This approach, feasible in model simulations akin to those presented by Kratter et al. (2008), is difficult to implement in numerical hydrodynamic simulations. Taking away matter and instantaneously transporting it over a large distance in the numerical grid may lead to numerical instabilities of unknown consequences. One possible way around this problem is to actually create fragments and follow their dynamics. However, when disk self-gravity is absent, this approach is also misleading because the dynamics of such fragments is largely governed by the gravitational interaction with the disk.

On the other hand, our viscous models demonstrate that the fragmentation regime is sometimes achieved in the early disk evolution (see e.g. Figure 7) and some changes to the standard effective-viscosity approach are necessary. In the present work, we modify the α -parameter so as to mimic a possible increase in the efficiency of mass transport due to fragmentation. In particular, in the Kratter et al.'s (2008) formulation of a_{GI} we have made the following modification to the short component

$$\alpha_{\text{short},f} = \alpha_{\text{short}} \left(\frac{Q_{\text{cr},f}}{Q_{\text{T}}} \right)^n, \quad (21)$$

if the fragmentation regime with $Q_{\text{T}} \leq Q_{\text{cr},f}$ is set in the disk. In the usual regime of $Q_{\text{T}} > Q_{\text{cr},f}$, the short component is not modified, i.e. $\alpha_{\text{short},f} = \alpha_{\text{short}}$. We set $Q_{\text{cr},f} = 1.0$ and $n = 10$, thus introducing a strong non-linearity in the expression for the α -parameter. We note that in the definition of α_{short} given by Equation (7), Q_{T} is not allowed to drop below unity by setting $Q_{\text{T}} = \max(Q_{\text{T}}, 1.0)$. In practice, this means that $(Q_{\text{cr},f}/Q_{\text{T}})^n$ is the only term that is sensitive to fragmentation.

Figure 12 presents a comparison of the KMK models with and without fragmentation with the SG model for the case of $\beta = 8.2 \times 10^{-3}$ and $\gamma = 1.4$.

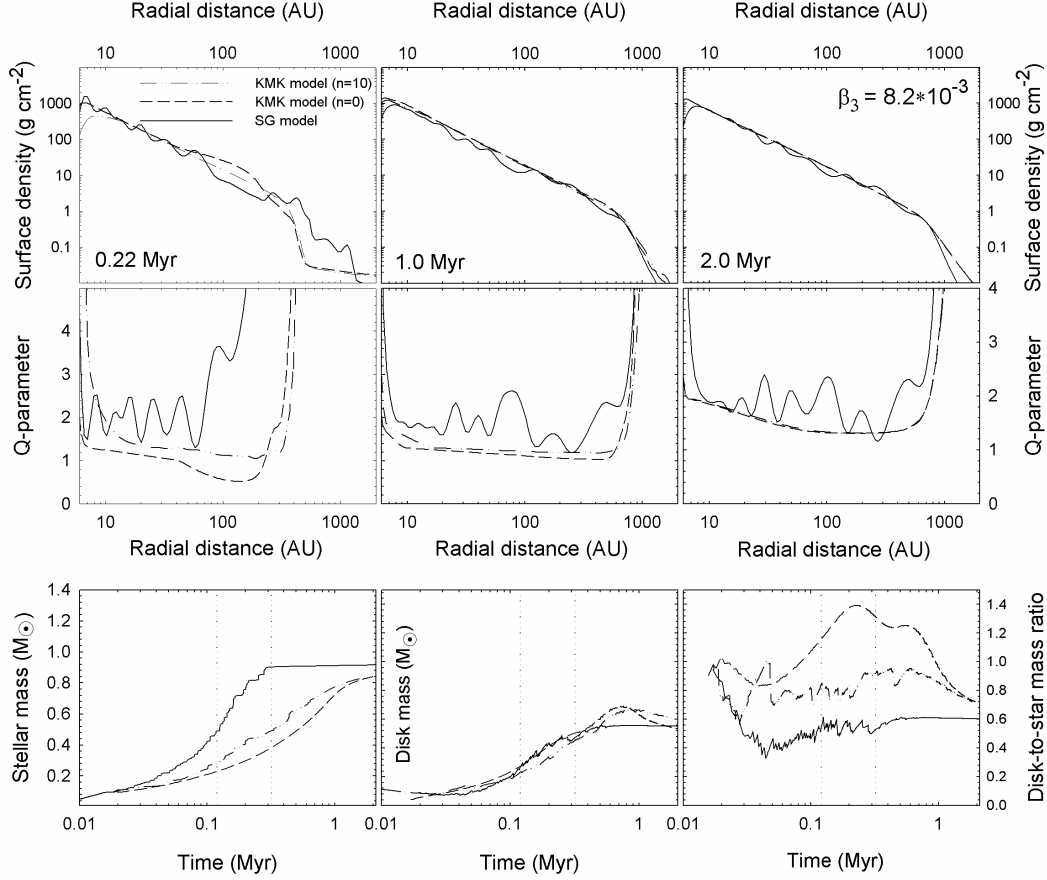


Fig. 12. Radial gas surface density profiles (top row) and Toomre Q-parameters (middle row) in the SG model (solid lines), unmodified KMK model (dashed lines), and modified-for-fragmentation KMK model (dash-dot-dotted lines). The bottom row presents the time evolution of the stellar mass (left panel), disk mass (middle panel), and disk-to-star mass ratio (right panel) in all three models.

The top and middle rows show the radial profile snapshots of the gas surface density and Q-parameter at three different times after the formation of the central star. The bottom row shows the time evolution of the stellar mass (left panel), disk mass (middle panel), and disk-to-star mass ratio (right panel). As usual, the solid and dashed lines represent the SG model and unmodified KMK model, respectively. The dash-dot-dotted line shows the KMK model modified for fragmentation. The vertical dotted lines mark the onset of the Class I and Class II phases in the SG model.

There are several interesting features in Figure 12 that deserve attention. When fragmentation is taken into account in the KMK model, the Q-parameter never dips appreciably below the critical value for fragmentation $Q_{\text{cr},f} = 1.0$, contrary to what was sometimes seen in the unmodified KMK model. This illustrates a self-regulating nature of the modification we have made to the standard KMK model. Furthermore, the modified KMK model reproduces better the exact solution, though the mismatch is still substantial. For in-

stance, the disk-to-star mass ratio in the modified KMK model is much closer to that of the SG model. In particular, the disk in the modified KMK model is almost always less massive than the star, which is in agreement with the expectations of the exact SG model (Vorobyov, 2009).

Perhaps, the most important feature of the modified KMK model is a non-monotonic, step-like increase in the mass of the central star with time, akin to that of the SG model. The disk-to-star mass ratios also demonstrates temporal variations similar to those of the SG model. We emphasize that the unmodified KMK model lacks such behaviour. These short-term variations are signatures of the mass accretion burst phenomenon. To illustrate this, we plot the instantaneous mass accretion rates \dot{M} versus time in Figure 13 for the unmodified KMK model (top), modified KMK model (middle), and SG model (bottom). The mass accretion rate in the unmodified KMK model exhibits only small-amplitude flickering, there is no trace of the several-orders-of-magnitude variability that is typical for the burst phenomenon. Much to our own surprise, the modified KMK model was found to have short-term variations in \dot{M} that are similar in amplitude to those of the SG model. Although the number of such bursts in the modified KMK model is still smaller than in the SG model, the mere fact that, after a simple modification, the KMK model can reproduce the burst phenomenon and accretion variability by several orders of magnitude is fascinating and encouraging.

7 Conclusions

We have performed numerical hydrodynamic simulations of the self-consistent formation and long-term (2 Myr) evolution of circumstellar disks with the purpose to determine the applicability of the viscous α -parameterization of gravitational instability in self-gravitating disks. In total, we have considered three numerical models: the LP model that uses the Lin & Pringle's (1990) α -parameterization, the KMK model that adopts the Kratter et al.'s (2008) α -parameterization, and the SG model that employs no effective viscosity but solves for the gravitational potential directly (the exact solution). We then perform a detailed analysis of the resultant circumstellar radial disk structure, masses, and mass accretion rates in the three models for systems with different disk-to-star mass ratios ξ . We find the following.

- (1) The agreement between the viscous α -models and the SG model depends on the value of ξ and deteriorates along the sequence of increasing disk-to-star mass ratios. In principle, the viscous α -models can provide an acceptable fit to the SG model for stellar systems with $\xi \lesssim 0.2 - 0.3$, which is in agreement with $\xi \leq 0.25$ previously reported by Lodato & Rice (2004) based on a different α -parameterization.

- (2) The success of the Lin & Pringle's α -parameterization in systems with $\xi \lesssim 0.2 - 0.3$ depends crucially on the proper choice of α_{LP} . The $\alpha_{\text{LP}} = 10^{-2}$ model yields an acceptable fit to the exact solution but completely fails for $\alpha_{\text{LP}} \lesssim 10^{-4}$ and $\alpha_{\text{LP}} \gtrsim 0.25$. In particular, the $\alpha_{\text{LP}} = 10^{-4}$ model yields a disk being too small in size, having too large gas surface density and disk-to-star mass ratio. On the other hand, the $\alpha_{\text{LP}} = 0.25$ model drives too large accretion rates, resulting in a disk being heavily depleted in mass and having too small gas-to-star mass ratios already after 1.0 Myr of evolution.
- (3) The performance of the KMK model is comparable to or even better than that of the best $\alpha_{\text{LP}} = 10^{-2}$ LP model. In addition, the former is superior because it has no explicit dependence on the α -parameter, and it includes some dependence on the disk-to-star mass ratio.
- (4) The viscous α -models generally fail in stellar systems with $\xi \gtrsim 0.3$. They yield too small stellar masses and too large disk-to-star mass ratios, especially in the early Class 0 and Class I evolution phases (see Table 1). For instance, the KMK model may overestimate the disk-to-star mass ratio by a factor of 3 as compared to that of the SG model. The same lack of agreement is also seen in the time-averaged mass accretion rates $\langle \dot{M} \rangle$. In particular, the KMK model underestimates $\langle \dot{M} \rangle$ in the Class 0 and Class I phases, while greatly overestimating $\langle \dot{M} \rangle$ in the Class II phase.
- (5) The failure of the KMK model (and LP model) in the case of large ξ is related to the growing strength of low-order spiral modes in massive self-gravitating disks.
- (6) A simple modification to the α -parameter that takes into account disk fragmentation can somewhat improve the performance of the KMK model and even reproduce to some extent the mass accretion burst phenomenon (Vorobyov & Basu, 2005; Vorobyov & Basu, 2006), demonstrating the importance of the proper treatment for disk fragmentation. More numerical study is needed to explore this issue.
- (7) Both viscous α -models perform better in the late disk evolution (Class II phase) than in the early disk evolution (Class 0 and Class I phases), irrespective of the value of ξ . This is due to a gradual decline in the magnitude of the spiral modes with time, as well as due to growing mode-to-mode interaction. The latter tends to produce more cancellation in the net gravitational torque on large scales, thus making the effect of gravitational torques similar to that of local viscous torques.
- (8) A factor of 2 increase in the disk temperature does not noticeably affect the efficiency of the viscous α -models in simulating the effect of GI.

Acknowledgements

The author is thankful to the anonymous referee for an insightful report that helped to improve the manuscript and to Prof. Shantanu Basu for stimulating discussions. The author gratefully acknowledges present support from an ACEnet Fellowship. Numerical simulations were done on the Atlantic Computational Excellence Network (ACEnet).

References

- Adams, F. C., Ruden, S. P., Shu F. H., 1989, *ApJ*, 347, 959
- André, P., Ward-Thompson, D., & Barsony, M. 1993, *ApJ*, 406, 122
- Andrews, S. M., Williams, J. P., 2005, *ApJ*, 631, 1134
- Andrews, S. M., Williams, J. P., 2007, 659, 705
- Balbus, S. A., Papaloizou, J. C. B., 1999, 521, 650
- Basu, S., 1997, *ApJ*, 485, 240
- Boley, A. C. 2009, *ApJL*, 695, 53
- Boss, A., 2001, *ApJ*, 563, 367
- Cai, K., Durisen, R. H., Boley, A. C., Pickett, M. K., Mejía, A. C. 2008, *ApJ*, 673, 1138
- Caselli, P., Benson, P. J., Myers, P. C., & Tafalla, M. 2002, 572, 238
- Cossins, P., Lodato, G., Clarke, C. J. 2009, *MNRAS*, 393, 1157
- Dullemond, C. P., Natta, A., Testi, L., 2006, *ApJ*, 645, L69
- Enoch, M. L., Evans, N. J. II, Sargent, A. I., Glenn, J., 2009, *ApJ*, 692, 973
- Gammie, C. F., 2001, *ApJ*, 553, 174
- Hayashi, C., Nakazawa, K., Nakagawa, Y.: in *Protostars and Planets II*. Tucson, AZ, University of Arizona Press, 1985, 1100
- Hueso, R., Guillot, T., 2005, *A&A*, 442, 703
- Ida, S., Lin, D. N. C., 2004, *ApJ*, 604, 388
- Kratter, K. M., Matzner, Ch. D., Krumholz, M. R., 2008, *ApJ*, 681, 375
- Krumholz, M. R., Klein, R. I., & McKee, C. F. 2007, *ApJ*, 656, 959
- Laughlin, G., Bodenheimer, P., 1994, *ApJ*, 436, 335

Laughlin, G., Rózyczka, P., 1996, ApJ, 456, 279

Laughlin, G., Korchagin, V., Adams, F. C., 1997, ApJ, 477, 410

Lin, D. N. C., Pringle, J. E., 1987, MNRAS, 225, 607

Lin, D. N. C., Pringle, J. E., 1990, ApJ, 358, 515

Lodato, G., Rice, W. K. M., 2004, MNRAS, 351, 630

Lodato, G., Rice, W. K. M., 2005, MNRAS, 358, 1489

Lodato, G., 2008, New Astronomy Reviews, 52, 41

Lynden-Bell, D., Pringle, J. E., 1974, MNRAS, 168, 603

Masunaga, H., Inutsuka, S. 2000, ApJ, 531, 350

Matzner, C. D., Levin, Yu., 2005, ApJ, 628, 817

Nakamoto, T., Nakagawa, Y., 1995, ApJ, 445, 330

Pringle, J. E., 1981, ARA& A, 19, 137

Shakura, N. I., Sunyaev, R. A., 1973, A&A, 24, 337

Shu, F. H. 1977, ApJ, 214, 488

Shu F. H., Tremaine S., Adams F.C., Ruden S. P., 1990, ApJ, 358, 495

Stamatellos, D., & Whitworth, A. P., 2008, A&A, 480, 879

von Neumann, J., Richtmyer, R. D., 1950, J. Appl. Phys., 21, 232

Vorobyov, E. I., & Basu, S. 2005, ApJL, 633, L137

Vorobyov, E. I., & Basu, S. 2006, ApJ, 650, 956

Vorobyov, E. I., & Basu, S. 2007, MNRAS, 381, 1009

Vorobyov, E. I., Basu, S., 2008, ApJ, 676, L139

Vorobyov, E. I., Basu, S., 2009, MNRAS, 393, 822

Vorobyov, E. I., 2009, ApJ, 692, 1609

Weidenschilling, S. J., 1977, Ap&SS, 51, 153